Relation between lattice order and energy-resolved momentum densities in carbon films

M. Vos,* P. Storer, Y.Q. Cai, I.E. McCarthy, and E. Weigold†
Electronic Structure of Materials Centre, Flinders University of South Australia, GPO Box 2100, Adelaide, South Australia 5001, Australia
(Received 25 May 1994; revised manuscript received 25 July 1994)

The $(e, 2e)$ technique is well known to be able to measure the momentum profiles of the electron orbitals in molecules. In crystalline solids energy levels are replaced by bands, and the momentum profiles simplify to energy-dependent δ functions. In this paper the development from a molecular to a crystalline picture of the electronic structure is illustrated using a simple model of a linear chain of atoms of increasing length. From this model we try to get some insight into the $(e, 2e)$ momentum profiles expected for disordered solids. These results are compared to the experimental data for carbon films with different degrees of order, i.e., amorphous carbon films, annealed amorphous carbon films, and highly oriented pyrolitic graphite (HOPG) films. The intensity of the π-electron contribution is suppressed in HOPG, due to the orientation chosen. In the annealed evaporated samples, the planes of graphite atoms have random orientation and the π electrons are clearly seen. With increasing order the momentum profiles show increasingly well defined peaks.

I. INTRODUCTION

In an $(e, 2e)$ measurement, an incoming electron ionizes the target and the scattered and ejected electrons are detected in coincidence. A well collimated monoenergetic electron beam (energy E_0, momentum $\mathbf{k}_0$) impinges on a target. Some of these electrons will be scattered over large angles by a collision with a target electron. In the case of high momentum transfer collisions, this process is well described as a binary collision between the scattered and ejected (target) electrons and is quantitatively well understood.[1] Due to the energy transfer the target electron is ejected. In our case, we use 20 keV incoming electrons, and detect electrons at 14° (energies of the detected electrons around 18.8 keV) and 76° (energies around 1.2 keV). We detect both scattered and ejected electrons *in coincidence* and determine their energies and momenta (E_s and $\mathbf{k}_s$ for the slower electron, E_f and $\mathbf{k}_f$ for the faster one). We choose $\hbar = 1$, thereby equating momentum and wave numbers. A comparison of the momentum and energy of the scattered and ejected electron with the momentum and energy of the incident electron gives us the magnitude of the momentum and binding energy of the ejected electron *before* the collision. At high enough energies, the free electrons can be treated as plane waves. We can infer the binding energy ε,

$$\varepsilon = E_0 - E_s - E_f, \tag{1}$$

and, the recoil momentum $\mathbf{q}$ which in the plane wave approximation is equal and opposite to the momentum of the target electron before the collision:

$$\mathbf{q} = \mathbf{k}_0 - \mathbf{k}_s - \mathbf{k}_f. \tag{2}$$

In our spectrometer, we measure in both detectors a range of azimuthal angles. For the choice of polar angles and energies mentioned above, the recoil momentum will be zero if $\mathbf{k}_0$, $\mathbf{k}_s$, and $\mathbf{k}_f$ are all in the same plane. If we define a scattering plane by the vectors $\mathbf{k}_0$ and $\mathbf{k}_s$, then the measured target electron momentum is directed approximately perpendicular to this plane, with a magnitude proportional to the component of $\mathbf{k}_f$ out of this plane. The range of azimuthal angles measured is ±7° in the toroid and ±18° in the hemisphere. This means that we can measure momenta from zero up to 3.5 atomic units (a.u.) in the direction perpendicular to the incoming electrons. (One atomic unit corresponds to 1.89 Å^{-1}.) In practice not much intensity is expected above two atomic units, for valence band measurements.

Thus, a complete description of the kinematics of the ionizing event is obtained. This technique has been used with great success in "wave function mapping" of atoms and molecules.[1] One obtains the momentum distribution $|\phi(\mathbf{q}, \varepsilon)|^2$ for the different discrete energies of the electronic orbitals of the atom or molecule. As an example, we show in Fig. 1 measurements for an Ar gas target.[2,3] The $3s$ electron in argon (binding energy 29.3 eV) has maximum intensity for zero momentum. This is true for all s type orbitals. For the Ar $3p$ orbitals (binding energy 15.8 eV) (and all p type orbitals) zero intensity is expected for zero momentum. The measured intensity at zero momentum in this case is a consequence of the finite momentum resolution of the experiment. The dashed lines in these figures are the calculated momentum densities $|\phi(\mathbf{q}, \varepsilon)|^2$, i.e., the expected results of the measurement with very good momentum resolution. The solid line includes the effects of the finite experimental momentum resolution. Note that the intrinsic width of the distribution is considerable, about 1 a.u.

In molecules, the number of occupied energy levels increases as the size of the molecule increases. For larger and larger molecules, the spacing in energy of the different orbitals becomes smaller and smaller. If the molecule

created in this way consists of repeating units, it starts resembling a crystal. If the energy separation of the different orbitals becomes much smaller than the energy resolution of the spectroscopy used (or equivalently, the properties of the molecule are not expected to change if one more unit is added), the electronic structure can be described using the band picture. It will be shown that the momentum distribution at each energy starts to resemble a δ function. This is a consequence of the long range order in crystals. For disordered solids, one would expect the momentum distribution at each energy to have finite width. As a very simple model, one can describe a disordered solid as a polycrystalline one. For small crystallites, the momentum distribution would be significantly broadened. It could be argued that the momentum densities of these polycrystalline solids can in first approximation be described as the sum of the densities of small (noninteracting) crystallites (i.e., consider each crystallite as a large molecule). As an example of a solid to which the above picture may apply, we present data of amorphous (evaporated) carbon films, annealed amorphous carbon films, and highly oriented pyrolitic graphite (HOPG) films. The annealed amorphous carbon films can be described by terms such as "turbostratic" graphite and "glassy" carbon.[4] They are thought to consist of sheets of single layers of graphite, with no ordering in between the layers. Electron diffraction of annealed evaporated films shows well defined rings[5] indicative of a fair amount of ordering. Thus with annealing the order in the evaporated films increases, and it will be shown that this is accompanied by a sharpening of the momentum distributions. Attempts have been made to calculate the electronic structure of amorphous carbon (see Ref. 4) as well as turbostratic carbon.[6] Unfortunately the results of these calculations are not presented in terms of energy-resolved momentum densities, so they cannot be compared directly with the experiments described here.

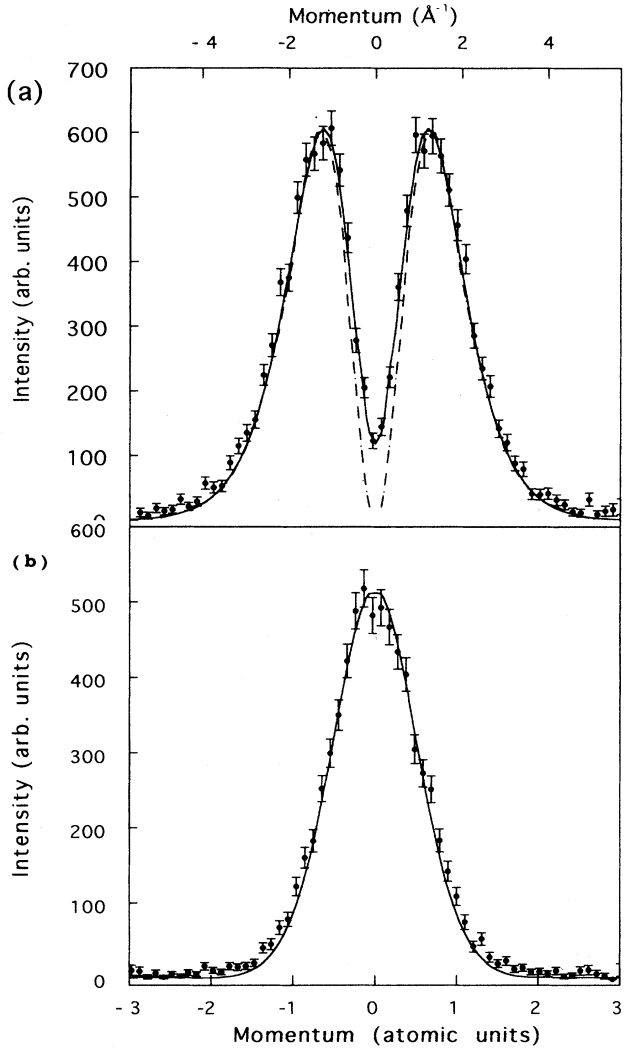

FIG. 1. The electron momentum densities for the 3s and 3p levels of argon, as measured by $(e, 2e)$. The dashed lines are the theoretical momentum densities for the Ar 3s and 3p level. The full line is obtained by folding the theoretical data with the experimental momentum resolution. These data were taken under identical conditions as the solid $(e, 2e)$ measurements. The momentum resolution for a gas target is expected to be less than the one for solids, due to the finite extent of the gas jet.

As a caveat, it should be noted that different approaches to the description of these films are possible. Amorphous carbon films can be described as containing partly threefold (sp^2 hybridized) and fourfold (sp^3 hybridized) atoms. Changes in the momentum densities could be described as a consequence of changes in the ratio of both contributions. Another approach is to focus on changes in the differences in overlap between atomic orbitals, due to variations in the interatomic distances in disordered solids. To what extent these approaches are mutually exclusive, is a question that will not be addressed here. The main point of this paper is to stress the fact that energy-resolved momentum densities of different carbon films are strikingly different, much more so than their momentum integrated energy density of states. Thus, we want to establish that $(e, 2e)$ spectroscopy is uniquely well suited for the probing of the electronic structure of amorphous materials. The theoretical argument is an attempt to get some intuition for the underlying physics.

The remainder of the paper is organized as follows. In Sec. II we describe the theory of $(e, 2e)$ for crystals. Subsequently we study the transition from "molecular" to "solid" behavior for a long molecule, and derive from this some insight into the expected behaviour of disordered solids. This is followed by experimental results for carbon films with different degrees of order. The extent to which the developed picture applies is discussed. A detailed description of the spectrometer has been published elsewhere[2] and is not given here. In another paper, we have already described $(e, 2e)$ measurements of the HOPG film, its preparation method, and a comparison with band structure calculations.[7] Here we focus on the influence of disorder on $(e, 2e)$ spectra.

Earlier attempts to study the electronic structure of both graphite and amorphous carbon by $(e, 2e)$ have been made.[8–11] These attempts were hampered by exceedingly

low countrates, and energy and momentum resolution of the order of the differences between the electronic structures of these samples. With the new spectrometer used here, these problems are largely overcome. Typical data acquisition time for each sample was four days.

II. SIMPLE THEORY OF $(E, 2E)$ ON A CRYSTAL

At the high energy of the present experiment, we approximate the wave function of the unbound electron by plane waves. A full analysis using the wave functions of dynamic diffraction theory has been given by Allen, McCarthy, Maslen, and Rossouw.[12] The differential cross section for ionization is[12]

$$\frac{d^5\sigma}{d\Omega_f\, d\Omega_s\, dE_f} = (2\pi)^4 N \frac{k_f\, k_s}{k_0} f_d\, f_{ee}\, |\Phi_{\mathbf{k}}(\mathbf{q})|^2, \qquad (3)$$

where N is the number of unit cells involved in the reaction, f_d is a dispersion factor,[13] which is close to one in most applications, and f_{ee} is the Mott scattering cross section for the two electrons. In the present experiment, all these factors are essentially constant.

The cross section depends sensitively on the momentum-space wave function of the struck electrons $\Phi_{\mathbf{k}}(\mathbf{q})$ where $\mathbf{q}$ is the momentum coordinate and $\mathbf{k}$ is the crystal momentum. Here, we are approximating the overlap of the initial and final state of the crystal by the independent particle model. The coordinate-space wave function of an electron with crystal momentum $\mathbf{k}$ and binding energy $\varepsilon(\mathbf{k})$ is

$$\Psi_{\mathbf{k}}(\mathbf{r}) = N^{-1/2} \sum_n \exp(i\mathbf{k}\cdot\mathbf{R}_n)\, \psi(\mathbf{r}-\mathbf{R}_n), \qquad (4)$$

where $\mathbf{R}_n$ is a lattice vector and $\psi(\mathbf{r})$ is the unit-cell wave function. The corresponding momentum-space wave function is given for a very large crystal by

$$\begin{aligned}\Phi_{\mathbf{k}}(\mathbf{q}) &= (2\pi)^{-3/2} \int d\mathbf{r} \exp(-i\mathbf{q}\cdot\mathbf{r})\, \Psi_{\mathbf{k}}(\mathbf{r}) \\ &= N^{1/2}\, \phi(\mathbf{q})\, \delta_{\mathbf{q},\,\mathbf{k}+\mathbf{G}}, \end{aligned} \qquad (5)$$

where $\mathbf{G}$ is an arbitrary reciprocal lattice vector, and

$$\phi(\mathbf{q}) = (2\pi)^{-3/2} \int d\mathbf{r} \exp(-i\mathbf{q}\cdot\mathbf{r})\, \psi(\mathbf{r}), \qquad (6)$$

is the momentum-space wave function of the unit cell.

Note that from Eq. (2), the observed momentum $\mathbf{q}$ is the real momentum of the target electron. This has an important influence on the interpretation of Eq. (5), which predicts that the momentum profile of the $(e, 2e)$ cross sections for different values of $\varepsilon(\mathbf{k})$ will be given by a series of δ functions modulated by the momentum density, $|\phi(\mathbf{q})|^2$. Although the δ functions may appear at values $\mathbf{q} = \mathbf{k} + \mathbf{G}$ where $\mathbf{G}$ is an arbitrary reciprocal lattice vector, they will, in general, have zero or nearly zero intensity for all but one value of $\mathbf{q}$ because of the modulation by $|\phi(\mathbf{q})|^2$.

The differential cross section, with the above approximations, is a direct measure of the momentum density $|\phi(\mathbf{q})|^2$. The approximations can be relaxed by considering inelastic events (such as plasmon creation), diffraction, and the finite size of crystals in the target used.

Inelastic events can be simply approximated by adding imaginary parts to the wave number of the plane waves, given by the inelastic mean free path of an electron of the corresponding energy. This makes almost no difference to the shape of the Fourier transform (6), but introduces an attenuation factor that depends on the experimental geometry. In our experiment, it results in the observed ionization collision without inelastic energy losses being concentrated near the exit surface of the target. Events that are accompanied by additional energy losses cause in the experiment a background that extends to higher binding energies.

In a simple static model, diffraction causes a reciprocal lattice vector $\mathbf{G}$ to be added to one of the incoming or outgoing momentum vectors in Eq. (2). This has the effect of reducing the measured intensity at certain values of $\mathbf{q}$ by shifting that intensity to a real momentum $\mathbf{q} + \mathbf{G}$. The effect of these "Umklapp processes" on the measured cross section is given by the different diffraction amplitudes that apply to the incoming and outgoing electrons. Such effects have not been identified in the present experiments.

Effects of the finite size of the crystal have been investigated by considering a one dimensional model. We have calculated the occupied molecular orbitals (with σ symmetry) in the self-consistent field approximation for a linear chain of N hydrogen atoms, with interatomic distances equal to the real H_2 molecule, using a linear combination of basis atomic orbitals appropriate to the hydrogen molecule. This enables us to explore how the molecular picture, which has a momentum distribution for each orbital with a main peak of significant width, develops into the crystal picture in which the momentum distribution for each orbital (characterized by $\mathbf{k}$) is a δ function.

The momentum distribution in the direction of the chain for each orbital is plotted in Fig. 2 for N=2, 4, 8, 12, 16, 24, 32. The distributions are shifted vertically with respect to each other by an amount corresponding to the binding energy of each level. With increasing N the energy levels of the molecular orbitals are more closely spaced. Their energy density is larger for larger binding energies, which corresponds to smaller momenta as expected for σ symmetry. The momentum distributions display a peak for each energy level, whose sharpness increases with N. The peaks occur at momenta that correspond to the crystal dispersion law as N increases. In our spectrometer the momentum resolution is 0.15 atomic units. Thus, we would barely be able to distinguish hydrogen chains of 24 units from an infinitely long chain. We expect that qualitatively the same is true for disordered solids. If the crystallites are smaller than 24 units along the momentum direction that we measure, we expect broadening of the momentum peaks. Note also that finite crystals exhibit nonzero momentum density at all momenta lower than the peak value. Because the spacing between levels is smallest at the bottom of the band, the momentum density per unit energy peaks at the bottom

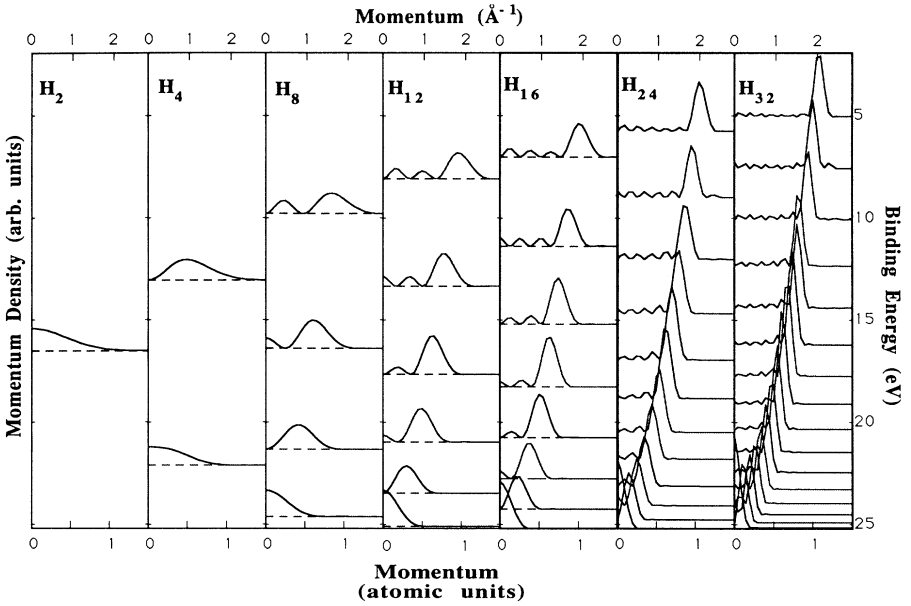

FIG. 2. Calculated momentum distributions for H_2 and the fictional H_4, H_8, H_{12}, H_{16}, H_{24}, and H_{32} (linear) molecules in the direction of the chain. The momentum density for each orbital is plotted with an offset proportional to its binding energy as indicated on the right vertical axis. With increasing chain length the momentum distributions are increasingly peaked, with the peak positions mimicking the dispersion relation of an infinitely long chain.

of the band, i.e., the electrons are most probable near the bottom of the band, around $\mathbf{q} \simeq 0$.

III. EXPERIMENTAL RESULTS

Because it is important to observe zero recoil momentum $(e, 2e)$ can best be done in a transmission geometry. The thickness of the film should be of the order of, or less than, the elastic and inelastic mean free path of the impinging electrons. The carbon films used in these experiments were obtained from Arizona Carbon Foil Co. Inc. and were nominally 80 Å thick. The films were floated off their glass supports in water and transferred to a Mo sample holder with several holes. On the as inserted films only a tiny amount of oxygen was detected by Auger spectroscopy. These films were heated in vacuum using electron beam annealing. Unfortunately this did not cause a uniform heating over the sample holder. From the experimental $(e, 2e)$ results it was clear that films in the center of the Mo sample holder were considerably warmer than films near the edge. In order to get some indication of the temperature, we spotwelded a thermocouple near the edge of the Mo sample holder. In this paper, we present results for two annealed films. One was located at the edge of the sample holder and heated with an electron beam power of 2 W. From the thermocouple reading, we estimate its temperature to be 600 °C. The other sample was located in the center and was annealed with 6 W electron beam power. We estimate that the temperature was at least 900 °C. Unfortunately, given the maximum allowable size of the sample holder, the necessity to transfer it in vacuum, and the restrictions due to the transmission geometry, accurate temperature measurement has presented difficulties.

In order to make a comparison of this anneal treatment with the anneal treatments in other experiments possible, we show the electron energy loss spectra of these films. These are presented in Fig. 3. From the ratio of the intensity of the loss structures to the elastic peak one can estimate the thickness of the samples. The HOPG sample was about twice as thick as the other three samples. For amorphous C, there is one broad loss structure centered around 25 eV, which shifts slightly to 23 eV after annealing. This is considerably lower than the plasmon loss maximum of HOPG (27 eV). A low plasmon loss energy has been attributed to low densities of the film.[14] For the annealed samples a second structure at about 7 eV energy loss develops. This feature is also seen in the energy loss spectra of the HOPG film. The high energy loss feature is attributed to plasmon oscillations of the σ and π electrons, whereas the feature at 7 eV is attributed to π electron plasma oscillation only[15] (for experiments in a transmission geometry one does not expect a significant contribution of surface plasmons). Annealing of amorphous, hydrogenated carbon films as published by Fink *et al.*[15] shows a similar development after annealing in the same temperature range. The development of this structure is seen as an indication for the formation of clear σ and π type bonds.

A lot of research has been done on the structure of different carbon films (see, e.g., Ref. 4). It is suggested that after annealing the carbon films can be described either as a random stacking of single graphite planes ("turbostratic graphite") or as an entanglement of graphitic ribbons ("glassy carbon"). It is not expected that the graphitic layers will order into true graphite until annealing temperatures exceeding 2000 °C.

In these experiments we measure the momentum along a specific direction perpendicular to the beam. The other two momentum components are (within experimental accuracy) zero. In Fig. 4, we present the results of the $(e, 2e)$ measurements integrated over all momenta along the measurement direction. In Fig. 4 differences between the four samples are marginal and it is difficult to interpret these differences in a convincing way. In fact, from

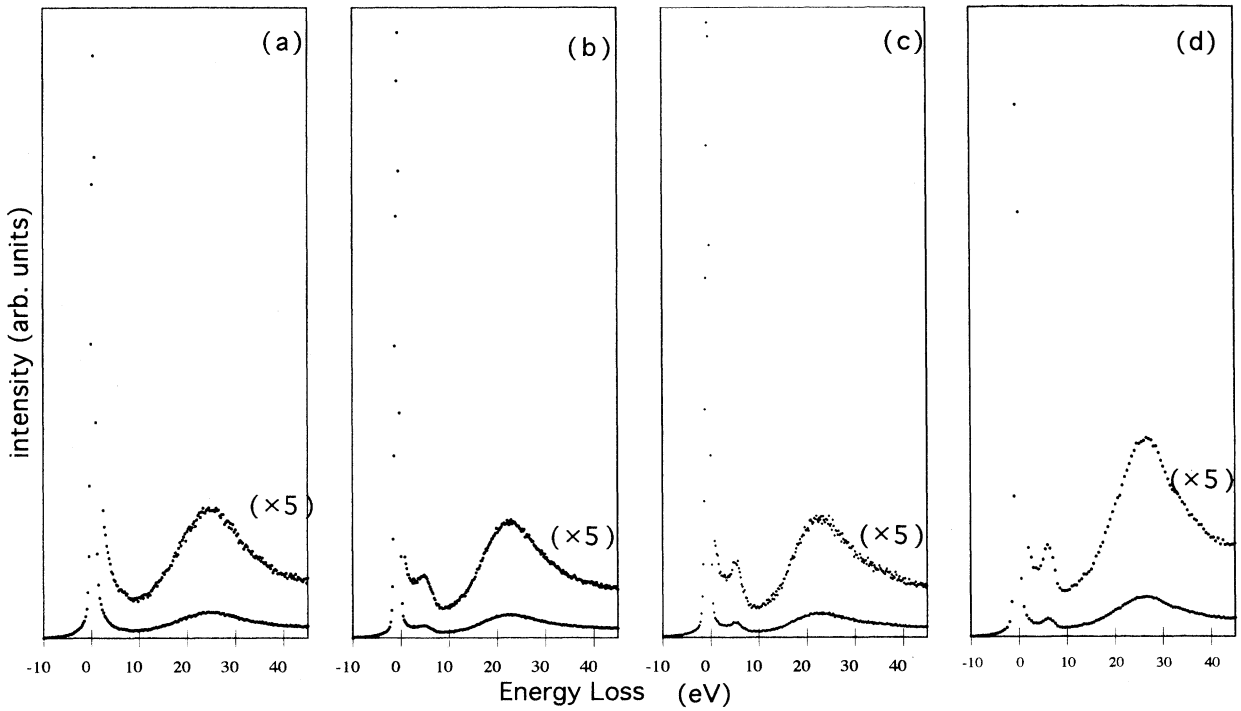

FIG. 3. The electron energy loss spectra for (a), an amorphous carbon film, (b) an amorphous C film annealed at low temperatures, (c) an amorphous C film annealed at high temperatures, and (d) the energy loss spectrum of a film of highly oriented pyrolitic graphite.

these data, one would argue that the four samples are strikingly similar. From the simple theory presented here one would expect that the $(e, 2e)$ intensity would drop to zero for binding energies larger than the valence band minimum ($\simeq$ 27 eV). In reality some of the incoming and outgoing electrons may be scattered elastically by the nuclei or be scattered inelastically (mainly plasmon excitations). Thus, the measured intensity is due to "clean" $(e, 2e)$ events on a smooth background of $(e, 2e)$ events in which one of the electrons involved have experienced additional elastic and/or inelastic scattering events. This is the reason that the intensity does not drop to zero at binding energies below the bottom of the σ band. The contributions due to inelastic energy loss can be removed by deconvolution.[16] In Fig. 5, we have done this deconvolution for the case of amorphous carbon. After deconvolution the spectral intensity is *not* simply the density of states of the solid. For isotropic solids, it is possible to obtain the true density of states $\rho(E)$ from the $(e, 2e)$ measurements by adding them weighted by $\mathbf{q}^2$. That is

$$\rho(\varepsilon) = \int_0^\infty |\phi(q)|^2 q^2 dq. \tag{7}$$

This result is shown in Fig. 5 as a well. Features near the Fermi edge are enhanced because, as will be shown, they correspond to larger $\mathbf{q}$ values. For anisotropic solids like HOPG, one would have to measure the momentum densities in all directions in order to obtain a true density of states, which is not feasible with the present spectrometer. X-ray-photoemission spectroscopy (XPS) measurements, although not obtaining a direct measure-

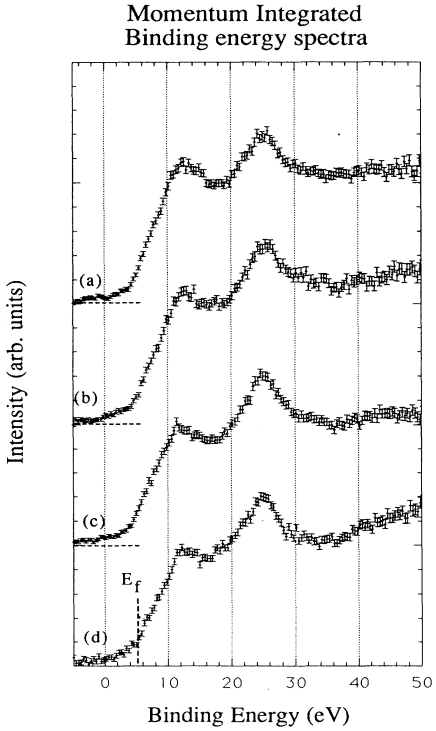

FIG. 4. The momentum integrated $(e, 2e)$ spectra for (a) amorphous carbon, (b) low-temperature annealed amorphous carbon, (c) high-temperature annealed amorphous carbon, and (d) highly oriented pyrolitic graphite. Note that these spectra differ only in details. Binding energies are expressed relative to the vacuum level, with the approximate position of the Fermi level indicated in the figure.

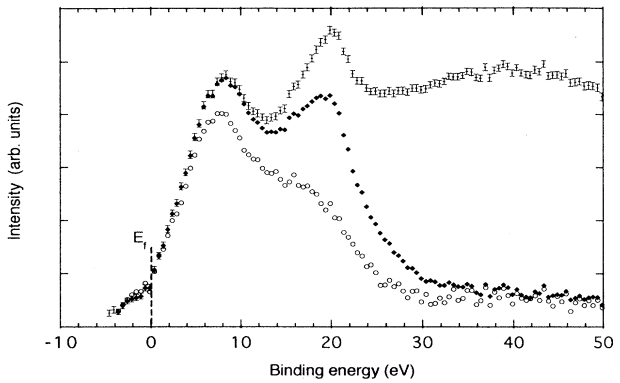

FIG. 5. Calculation of the density of states of unannealed amorphous carbon from the momentum integrated spectra. The momentum integrated raw data (error bars) have been deconvoluted for inelastic energy losses (filled squares). The open circles correspond to the q^2 weighted momentum integrated spectrum, which is the experimental estimate of the valence band density of states. The binding energy in this figure is relative to the Fermi level.

ment of the energy density of states, give information which in some respects can be regarded as similar to that shown in Fig. 5. X-ray-photoemission spectroscopy valence band spectra of amorphous graphite and HOPG [although taken with better energy resolution than these $(e, 2e)$ measurements] look roughly the same.[17]

The situation changes, however, if we look at the momentum-resolved $(e, 2e)$ spectra. These are presented as plots in Fig. 6. The vertical scale is energy, the horizontal one the momentum. The pictures should be symmetric with respect to zero momentum. Intensity is indicated in a gray scale. The lighter the shading, the higher the intensity. The easiest way of understanding these pictures is to start with the one for highly oriented pyrolitic graphite [Fig. 6(d)]. The sample was oriented in the spectrometer in such a way that the momentum density of states was measured in the basal plane, where only the σ band should be visible.[7] The σ band is evident in Fig. 6(d) as a parabola. Binding energies are expressed relative to the vacuum level. The Fermi level in these plots is at about 5 eV. The shape and intensity of this parabola compare well with band structure calculations.[7]

For the amorphous carbon case 6(a), this parabola is smeared out considerably. There is still a clear maximum near zero momentum, but for increasing momenta the parabola fades out rapidly. Annealing of the film causes a gradual sharpening of the parabola. At binding energies of around 10 eV there is structure for the annealed amorphous samples that is absent in the HOPG one. These are the π electrons. Because the graphitic sheets have a random orientation the intensity of the π electrons is not supressed in these samples to the same extent as in HOPG.

To get a more quantitative insight into these spectra, we plot the momentum densities for selected energies. These are presented in Fig. 7. The plots shown were obtained by integrating over 3 eV wide energy bins, centered around the energies indicated in the plots. Integrating over 3 eV decreases the statistical error, at the expense of only a very slight broadening of the features. The momentum densities were normalized in such a way that the density at the bottom of the σ band (around 27 eV) is equal for all cases. For each energy, the plots have different vertical scales. For 27 eV binding energy (close to the bottom of the band), all samples have similar momentum densities. Clearly the dispersion curves

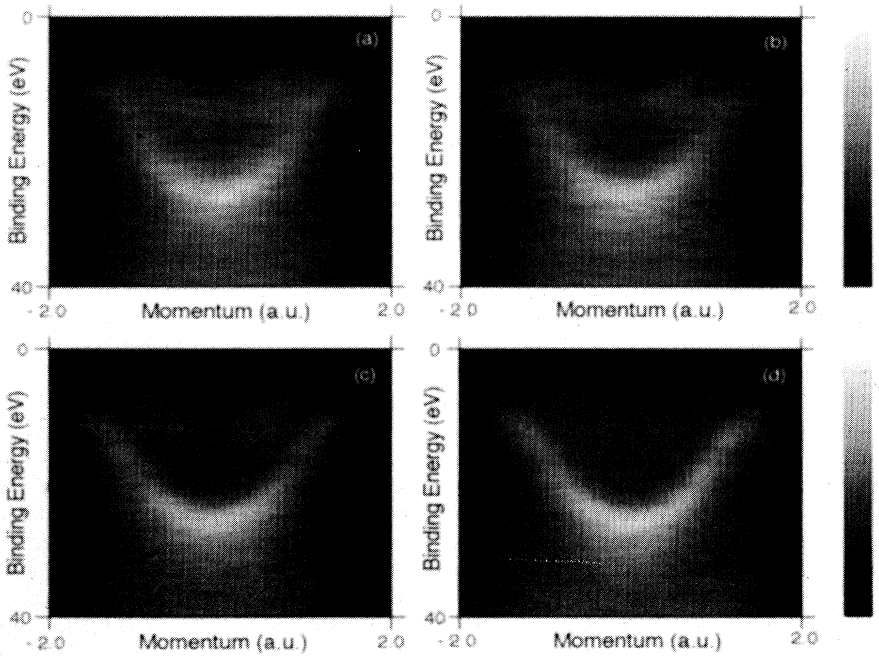

FIG. 6. The energy-resolved momentum density of states, plotted in gray scales for (a) amorphous carbon, (b) low-temperature annealed amorphous carbon, (c) high-temperature annealed amorphous carbon, and (d) HOPG. The lighter the shading the larger the intensity. In HOPG the region of highest intensity is a parabola. These represent the σ band. The same structure becomes more and more evident in the amorphous carbon data with increasing annealing temperature.

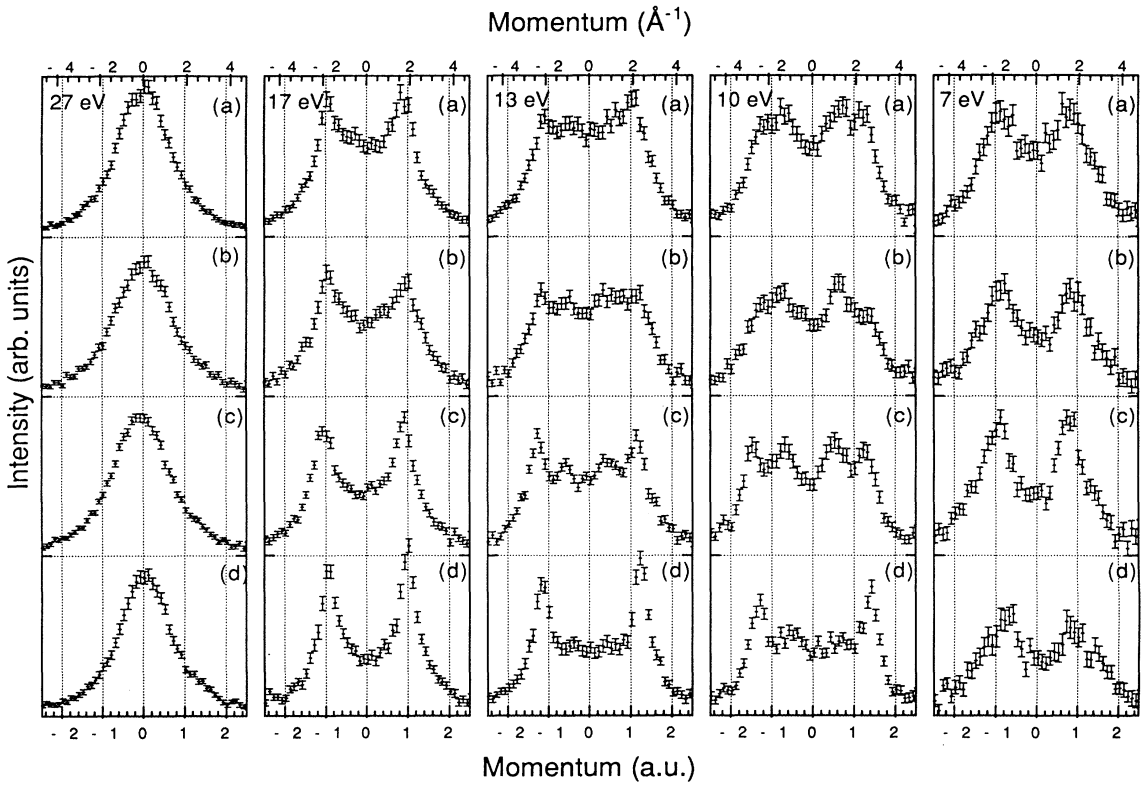

FIG. 7. Momentum densities for the energies indicated. All curves are normalized to have equal peak height at zero momentum and 27 eV binding energy. Each panel has a different vertical scale. The plots are for amorphous carbon (a), low-temperature annealed amorphous carbon (b), high-temperature annealed amorphous carbon (c), and HOPG (d). Away from zero momentum the momentum distributions show sharper peaks with increasing order.

are rather flat here (see Fig. 6), and as a consequence the widths of the momentum densities are determined more by the energy resolution than the sharpness of the momentum densities themselves. Moreover, these distributions correspond to small **k** values, where we are rather insensitive to the degree of disorder.

At 17 eV binding energy the situation is completely different. The amorphous sample before annealing shows some indication of the presence of two peaks at $\pm$ 1 a.u. momentum, but the intensity between the peaks is about 2/3 of the peak intensity. This peak-to-valley ratio slowly increases with annealing, together with some sharpening of the peaks. For HOPG the intensity between the two peaks is less than 1/3 of the peak value. Note that the peaks for HOPG at this and the following energy are much sharper than the Ar peaks in Fig. 1. They are also much sharper than the distributions for the $2p$ and $2s$ levels expected for carbon atoms. Thus, the sorting out of momentum with energy in a solid as described in the previous section can be confirmed experimentally. The widths of these peaks can be attributed completely to the experimental momentum resolution and (because of the dispersion) energy resolution. Much could be gained in $(e, 2e)$ measurements of solids by increasing the momentum resolution (presently 0.3 Å^{-1}), and there is not an intrinsic limit to the accuracy that can be obtained, as in gas phase $(e, 2e)$.

For 13 eV binding energy the peaks of the HOPG sample are still sharp; however, for the annealed amorphous carbon case there is more intensity between the peaks, compared to the 17 eV case, and the effect of annealing is less clear in this case. The reason for this is that this energy corresponds with the bottom of the π band. Because of the random orientation of the graphite sheets the intensity of the π electrons is not suppressed in this case as it is for HOPG.

Note that the peaks have slightly dispersed outward compared to the previous energy. At this binding energy, we are 14 eV above the bottom of the σ band. For a parabolic band, the dispersion at this energy would be $\sqrt{(14/10)} \simeq 1.2$ times larger than for the 17 eV binding energy (i.e., 10 eV above the bottom of the band) case. Indeed the peak position has shifted from 1.0 a.u. at 17 eV binding energy to 1.2 a.u. at 13 eV.

This is even more clear at 10 eV binding energy. We are now near the top of the σ band. For the HOPG sample, we still see the two peaks of the σ band. For the high temperature annealed sample there are clearly four peaks visible, two corresponding to the σ band (at about 1.3 a.u.) and two for the π band (at about 0.8 a.u.) [the latter two correspond to the second feature in Fig. 6(c)]. For the evaporated sample and to a lesser extent the low-temperature annealed one, these four peaks are not resolved, and the momentum density resembles two

broad bumps.

Finally, at 7 eV (just 2 eV below the Fermi level), we see no trace of the high momentum σ band anymore. After the high-temperature annealing the π electron momentum distribution has well defined peaks with three times the intensity of the valley at zero momentum. This peak-to-valley ratio was only 1.5 before annealing. Even the HOPG spectrum is dominated by π electrons with intensity peaking at about 0.9 a.u. (Ideally the intensity of the π electrons should be zero and the measured intensity has to be attributed to either finite momentum resolution or misalignment of the basal plane of the thin film due to wrinkling.) However, the peak intensity of the HOPG spectrum is less than the one for the high-temperature annealed case, showing that its intensity is suppressed compared to randomly oriented crystallites.

IV. CONCLUSION

Energy-resolved measurements of momentum distributions as measured by $(e, 2e)$ can provide us with detailed information about the electronic structure of amorphous and disordered solids, much more so than momentum integrated spectroscopies. The differences can be understood intuitively using simple models. Moreover, it is straightforward to obtain momentum densities as measured by $(e, 2e)$ from the wave functions generated by model calculations for these solids. Thus, $(e, 2e)$ measurements promise to be a good test of electronic structure calculations of disordered solids.

ACKNOWLEDGMENTS

The authors want to thank the technical staff of the Electronic Structures of Materials Centre for their indispensable contributions to the construction of the $(e, 2e)$ spectrometer. The Electronic Structure of Materials Centre is supported by a grant of the Australian Research Council.

* Electronic address: Phmv@cc.flinders.edu.au
† Present address: Research School of Physical Sciences and Engineering, Australian National University, Canberra, ACT 0200, Australia.

[1] I.E. McCarthy and E. Weigold, Rep. Prog. Phys. **54**, 789 (1991).
[2] P. Storer, S.A.C. Clark, R.C. Caprari, M. Vos, and E. Weigold, Rev. Sci. Instrum. **65**, 2214 (1994).
[3] I.E. McCarthy, R. Pascal, P. Storer, and E. Weigold, Phys. Rev. A **40**, 3041 (1989).
[4] J. Robertson, Adv. Phys. **35**, 317 (1983).
[5] L.B. Leder and J.A. Suddeth, J. Appl. Phys. **31**, 1422 (1960).
[6] J.-Charlier, J.-P. Michenaud, and Ph. Lambin, Phys. Rev. B **46**, 4540 (1992).
[7] M. Vos, P.J. Storer, S. Canney, A.S. Kheifets, I.E. McCarthy, and E. Weigold, Phys. Rev. B **50**, 5635 (1994).
[8] A.L. Ritter, J.R. Dennison, and R. Jones, Phys. Rev. Lett. **53**, 2054 (1984).
[9] C. Gao, A.L. Ritter, J.R. Dennison, and N.A.W. Holzwarth, Phys. Rev. B **37**, 3914 (1988).
[10] P. Hayes, J.F. Williams, and J. Flexman, Phys. Rev. B **43**, 1928 (1991).
[11] A.S. Kheifets, J. Lower, K.J. Nygaard, S. Utteridge, M. Vos, E. Weigold, and A.L. Ritter, Phys. Rev. B **49**, 2113 (1994).
[12] L.J. Allen, I.E. McCarthy, V.W. Maslen, and C.J. Rossouw, Aust. J. Phys. **43**, 453 (1990).
[13] V.G. Neudachim, G.A. Novoskol'tseva, and Yu.F. Smirnov, Zh. Eksp. Teor. Fiz. **55**, 1039 (1960) [Sov. Phys. JETP **28**, 540 (1969)].
[14] D.R. McKenzie, D. Muller, and B.A. Pailthorpe, Phys. Rev. Lett. **67**, 773 (1991).
[15] J. Fink, T. Müller-Heinzerling, J. Pflüger, A. Bubenzer, P. Koidl, and G. Creselius, Solid State Commun. **47**, 687 (1983).
[16] R. Jones and A.L. Ritter, J. Electron. Spectrosc. Relat. Phenom. **40**, 285 (1986).
[17] F.R. McFreely, S.P. Kowalczyk, R.G. Cavell, R.A. Pollak, and D.A. Shirly, Phys. Rev. B **9**, 5268 (1974).

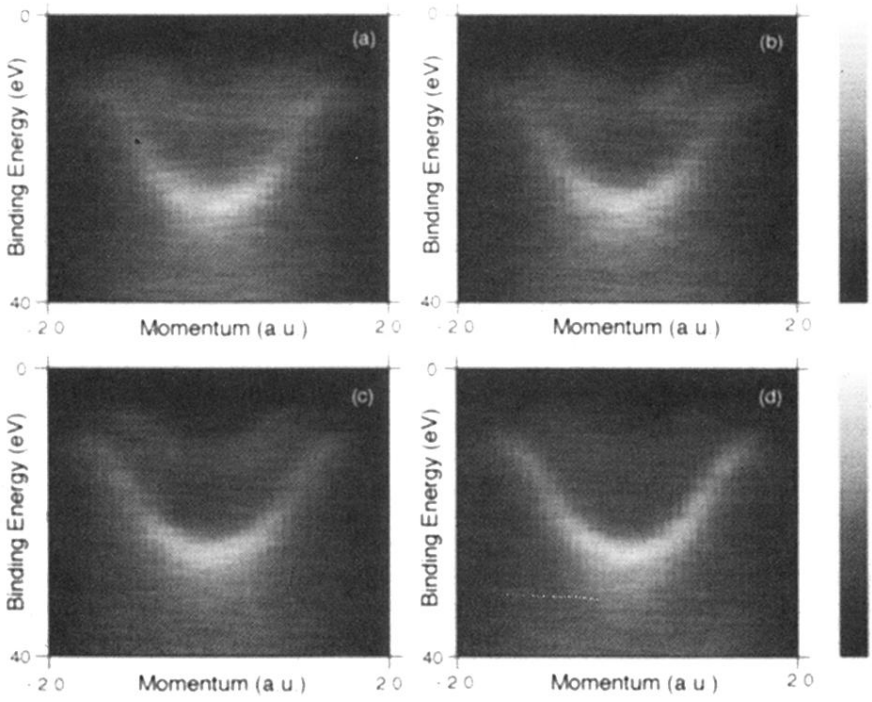

FIG. 6. The energy-resolved momentum density of states, plotted in gray scales for (a) amorphous carbon, (b) low-temperature annealed amorphous carbon, (c) high-temperature annealed amorphous carbon, and (d) HOPG. The lighter the shading the larger the intensity. In HOPG the region of highest intensity is a parabola. These represent the σ band. The same structure becomes more and more evident in the amorphous carbon data with increasing annealing temperature.